Si/SiGe quantum cascade superlattice designs for terahertz emission

G. Matmon,[1] D. J. Paul,[2,a)] L. Lever,[3] M. Califano,[3] Z. Ikonić,[3] R. W. Kelsall,[3] J. Zhang,[4] D. Chrastina,[5] G. Isella,[5] H. von Känel,[5] E. Müller,[6] and A. Neels[7]

[1]*Cavendish Laboratory, University of Cambridge, J. J. Thomson Avenue, Cambridge CB3 0HE, United Kingdom*
[2]*Department of Electronics and Electrical Engineering, University of Glasgow, Rankine Building, Oakfield Avenue G12 8LT, United Kingdom*
[3]*School of Electronic and Electrical Engineering, University of Leeds, Leeds LS2 9JT, United Kingdom*
[4]*Blackett Laboratory, Imperial College London, Prince Consort Road, London SW7 2BW, United Kingdom*
[5]*Dipartimento di Fisica del Politecnico di Milano, L-NESS, Polo Regionale di Como, Via Anzani 42, I-22100 Como, Italy*
[6]*Electron Microscopy, ETH Zürich, CH-8093 Zürich, Switzerland*
[7]*Institute of Microtechnology, University of Neuchâtel, CH-2002 Neuchâtel, Switzerland*

Quantum cascade lasers (QCLs) are compact sources that have demonstrated high output powers at terahertz (THz) frequencies. To date, all THz QCLs have been realized in III-V materials. Results are presented from $Si_{1-x}Ge_x$ quantum cascade superlattice designs emitting at around 3 THz which have been grown in two different chemical vapor deposition systems. The key to achieving successful electroluminescence at THz frequencies in a p-type system has been to strain the light-hole states to energies well above the radiative subband states. To accurately model the emission wavelengths, a 6-band $\mathbf{k} \cdot \mathbf{p}$ tool which includes the effects of nonabrupt heterointerfaces has been used to predict the characteristics of the emitters. X-ray diffraction and transmission electron microscopy have been used along with Fourier transform infrared spectroscopy to fully characterize the samples. A number of methods to improve the gain from the designs are suggested. © 2010 American Institute of Physics. [doi:10.1063/1.3319653]

The terahertz (THz) part of the electromagnetic spectrum (300 GHz to 10 THz) is presently being researched for applications including medical imaging,[1] security imaging,[2] production monitoring,[3] and astronomy.[4] While this part of the electromagnetic spectrum has been used for many decades to undertake spectroscopic research and identification of different molecules, it is only through the advent of practical THz systems in the last decade that the field has expanded enormously.[5] For most of the applications described above, a cheap, practical, high-power THz source which can operate at room temperature is required. This has not yet been achieved and the potential mass market applications for THz are unlikely to be achieved unless such a source can be realized.

Quantum cascade lasers (QCLs)[6] are one of the potentially practical THz sources which are presently being investigated.[7,8] To date all demonstrated THz QCLs have been fabricated in either GaAs or InGaAs heterostructures.[7,8] While impressive output powers of up to 248 mW have been demonstrated at 10 K,[9] the output powers decrease significantly when the temperature is increased.[10] The highest operating temperature is presently around 186 K which is still well below the practical range of Peltier coolers.[11] THz QCLs are unlikely to be cheap and practical in a complete system until operation with Peltier coolers at temperatures above ~220 K can be achieved.

Si/SiGe heterostructures[12] have also been investigated as practical THz sources.[13] While a laser has yet to be achieved,

THz emission has been demonstrated in a number of simple designs.[14–17] Si/SiGe heterostructures would have many significant advantages over III-V QCLs if a laser could be achieved. First the lasers could be fabricated on large Si wafers and processed using the cheap and mature Si process technology in Si foundries[12] which could significantly reduce the cost of the sources compared to III-V technology. Second, the lack of polar optical phonon scattering results in longer intersubband lifetimes at higher temperatures than in III-V materials (between 100 and 300 K) (Refs. 18–21) which could allow lasers to operate at higher temperatures.

To date, all THz emission from Si/SiGe quantum cascade designs has been achieved using p-type material.[13–17] High peak current density resonant tunneling has been demonstrated using tensile strained n-Si quantum wells with $Si_{0.4}Ge_{0.6}$ barriers at room temperature,[22,23] but the high effective mass (m^*) of ~0.93 m_0 (where m_0 is the free electron mass) makes the formation of minibands, which extend over many quantum wells and are used in most of the QCL designs[7,24] very difficult. Also Si/SiGe heterostructure growth is more mature for lower Ge contents[12] which is more amenable to p-type designs. THz emission has been demonstrated using intrawell[14,15] and interwell[16] heavy-hole (HH) to HH and light-hole (LH) to HH designs but the lack of any dedicated injector significantly reduced the injection efficiency into the upper radiative laser level[13] (strictly speaking the LH states are mixed LH/split off states but for brevity they will be called LH states in this paper). Phonon depopulation structures have also been attempted but such devices require extremely precise heterostructure growth

---

a)Electronic mail: D.Paul@elec.gla.ac.uk.

which is presently beyond the capabilities of Si/SiGe growth technology.[13,25]

In this paper, superlattice designs with a similar interwell transition active region to those which have achieved high temperature operation in III-V THz QCLs[11] are used in an attempt to demonstrate more efficient *p*-type Si/SiGe quantum cascade electroluminescence. Bound-to-continuum designs have previously been demonstrated in *p*-type Si/SiGe quantum cascades at midinfrared frequencies between a bound HH upper state to a lower HH superlattice miniband.[26] In this case, only weak electroluminescence was visible from the parasitic LH states between the radiative subband states. Similar designs for THz electroluminescence resulted in excellent current-voltage characteristics but the output powers were too weak to be measured above the blackbody emission from heating in the system. These results suggested that scattering to LH states prevented the observation of strong HH to HH electroluminescence.[13,25] In this paper, designs are presented in which the LH states are strained above the upper HH radiative state thereby removing transitions to the parasitic LH states and allowing electroluminescence to be measured. The benefit of pushing LH states upwards comes from the fact that, depending on the exact configuration of states, the deformation potential coupling between HH and LH states may be even stronger than between like types of hole states, and eliminating this very efficient channel for the upper HH state depopulation may significantly increase the hole lifetime therein, and hence the luminescence efficiency. The results demonstrate that this strain technique is essential to obtain electroluminescence from the samples. Two different superlattice designs are presented grown in two different growth systems to demonstrate the universality of the approach.

A 6-band $\mathbf{k} \cdot \mathbf{p}$ modeling tool[27] has been used along with a rate equation model, to determine the current and gain for each design.[28] Previous work has demonstrated that to accurately model the structures the nonabruptness of the heterointerfaces due to segregation and diffusion during growth needs to be considered.[28] As two different growth systems have been used for the two structures to be discussed below, different segregation lengths have been used. For sample 1 grown at the L-NESS in Como, a small segregation length of 0.1 nm has been estimated by comparing dynamical simulations to results from x-ray diffraction (XRD) measurements[29] while for sample 2 grown at Imperial College, a segregation length of 1.0 nm was used which was obtained from high-resolution transmission electron microscopy (TEM) measurements.[30]

Two different growth systems have been used for the two samples grown for this work (Fig. 1). Sample 1 was grown by low-energy plasma-enhanced chemical vapor deposition (LEPECVD) on a *p*-Si(001) substrate using SiH$_4$, GeH$_4$, and B$_2$H$_6$ as precursor gases.[31] An undoped graded Si$_{1-x}$Ge$_x$ buffer was grown at a grading rate of about 7%/μm up to a final Ge content of *x*=0.35, while the substrate temperature was gradually lowered from 760 to 550 °C. A 2 μm thick undoped constant composition buffer of Si$_{0.65}$Ge$_{0.35}$ was grown on top, followed by a 0.5 μm bottom contact of Si$_{0.65}$Ge$_{0.35}$ B-doped to 10^{19} cm^{-3}. The complete

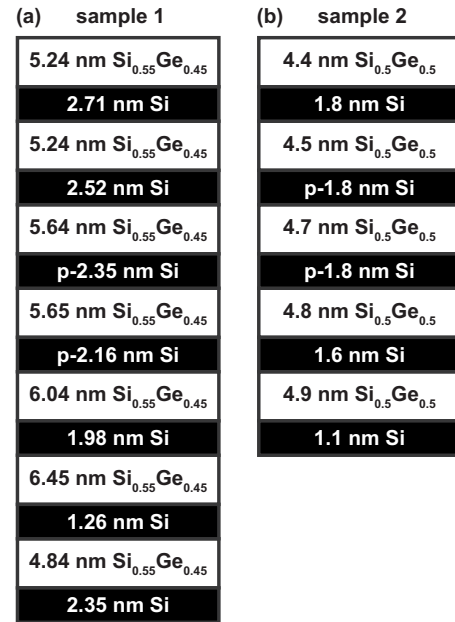| (a) sample 1	(b) sample 2
5.24 nm Si$_{0.55}$Ge$_{0.45}$	4.4 nm Si$_{0.5}$Ge$_{0.5}$
2.71 nm Si	1.8 nm Si
5.24 nm Si$_{0.55}$Ge$_{0.45}$	4.5 nm Si$_{0.5}$Ge$_{0.5}$
2.52 nm Si	p-1.8 nm Si
5.64 nm Si$_{0.55}$Ge$_{0.45}$	4.7 nm Si$_{0.5}$Ge$_{0.5}$
p-2.35 nm Si	p-1.8 nm Si
5.65 nm Si$_{0.55}$Ge$_{0.45}$	4.8 nm Si$_{0.5}$Ge$_{0.5}$
p-2.16 nm Si	1.6 nm Si
6.04 nm Si$_{0.55}$Ge$_{0.45}$	4.9 nm Si$_{0.5}$Ge$_{0.5}$
1.98 nm Si	1.1 nm Si
6.45 nm Si$_{0.55}$Ge$_{0.45}$	
1.26 nm Si	
4.84 nm Si$_{0.55}$Ge$_{0.45}$	
2.35 nm Si	

FIG. 1. (a) The heterolayer Ge contents and layer thicknesses for sample 1 in the active quantum cascade period. (b) The heterolayer Ge contents and layer thicknesses for sample 2 in the active quantum cascade period. In both cases the injection barrier is at the bottom of the heterostructure stack.

buffer was grown at a maximum rate of 10 nm/s. On top, a 44 nm Si$_{1-x}$Ge$_x$ injector was grown graded from 0.34 to 0.44 Ge content and B-doped at 10^{17} cm^{-3}. 100 periods of the following (nominal) structure were grown at an average deposition rate of 13 nm/min and at 550 °C, where bold numbers (normal text) are Si barriers (Si$_{0.55}$Ge$_{0.45}$) in nanometer: **2.35**, 4.84, **1.26**, 6.45, **1.98**, 6.04, **p-2.16**, 5.65, **p-2.35**, 5.64, **2.52**, 5.24, **2.71**, and 5.24. Two of the barriers were doped as indicated to provide a sheet charge density of 5×10^{11} cm^{-2}. The final capping layers were 2.35 nm Si, 5.03 nm Si$_{0.55}$Ge$_{0.45}$, 1.26 nm Si, 115 nm graded Si$_{1-x}$Ge$_x$ with *x* from 0.42 to 0.35 doped at 10^{17} cm^{-3}, 67 nm *p*-Si$_{0.65}$Ge$_{0.35}$ doped at 10^{19} cm^{-3}, and a 6.7 nm *p*-Si cap. All 1411 heterolayers with a total thickness of ~15 μm were grown in under 5 hours, demonstrating the advantage of the LEPECVD technique for growing the thick heterostructure stacks required for QCLs.

The heterolayer thicknesses for sample 1 have been extracted from TEM images and high resolution XRD measurements as shown in Figs. 2 and 3, respectively. The TEM image of Fig. 2 demonstrates the excellent uniformity of the heterolayers. TEM images from both the top and bottom (not shown) of the quantum cascade stack demonstrate less than 1% variation in the heterolayer thicknesses between the top
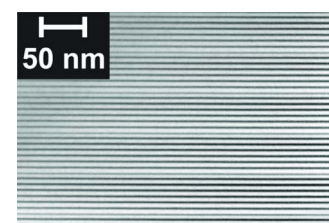

FIG. 2. (Color online) A TEM micrograph showing the top five periods of the first sample as taken in a Philips CM30 microscope.
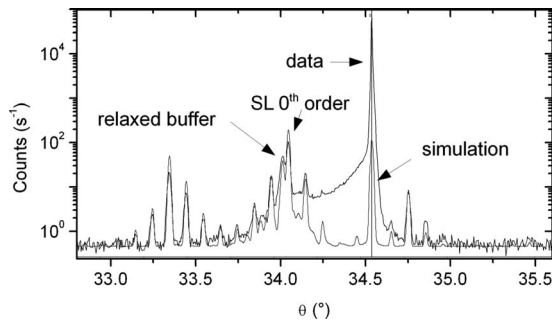
FIG. 3. A high resolution XRD $\omega-2\theta$ scan through the (004) reflection of the first sample. Dynamical simulations were used to extract the Ge content, strain state, and superlattice period.

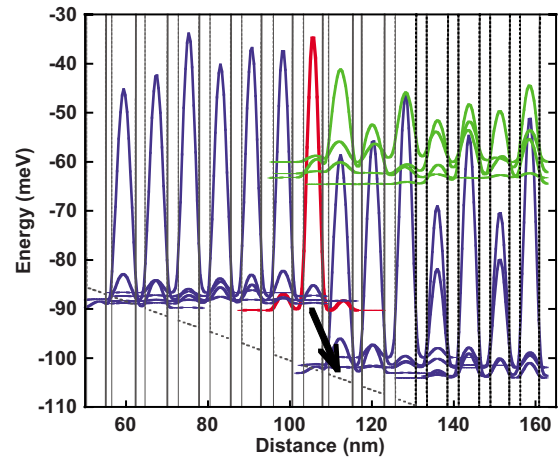

FIG. 4. (Color online) The band structure and squared envelope functions of sample 1 at 2.5 kV/cm as calculated by 6-band $\mathbf{k}\cdot\mathbf{p}$ theory. The HH states are blue, LH states are green, the upper radiative state is red, the HH band edge is solid black, and the LH band edge is dashed black. A Ge segregation length of 0.1 nm has been used in the simulations.

and bottom of the complete stack of 1400 heterostructures. The position of the relaxed buffer peak in the XRD spectra indicates that the virtual substrate is almost exactly the designed $Si_{0.65}Ge_{0.35}$. A small shift with respect to the zeroth order superlattice peak indicates that the strain symmetrisation through the complete heterolayer stack is not perfect, since the average x of the quantum cascade stack is not identical to the x of the virtual substrate.

The growth system used for sample 2 is a VG Semicon gas-source molecular beam epitaxy (GSMBE) system using Si_2H_6 and GeH_4 as the source gases along with B_2H_6 for p-type doping. The system can be run at two different pressures, allowing fast growth for strain relaxation buffers[12] in low pressure chemical vapor deposition mode using 2 Pa and 800 °C before being reduced to 6.7×10^{-3} Pa and 550 °C for the accurate growth of heterolayers in GSMBE mode.[32] The virtual substrate for the second sample consisted of ~3 μm of graded $Si_{1-y}Ge_y$ with y from 0.0 to 0.34 followed by ~1 μm of constant composition $Si_{0.66}Ge_{0.34}$ all grown on a p-Si(100) substrate. The design Ge content was 0.357 while a value of 0.34 was measured by XRD in the grown wafer. Next, a bottom contact of 400 nm of p-$Si_{0.66}Ge_{0.34}$ doped at 9×10^{18} cm^{-3} as measured by secondary ion mass spectrometry (SIMS) in calibration wafers was grown before changing to GSMBE mode for the active quantum cascade periods. A graded $Si_{1-x}Ge_x$ injector was grown from 0.34 to 0.50 doped at 1×10^{17} cm^{-3} before 30 periods of the active region quantum cascade design. The active heterolayer period sequence from left to right in nanometer starting from the injection barrier is **1.1**/4.9/**1.6**/4.8/p-**1.8**/4.7/p-**1.8**/4.5/**1.8**/4.4. Si barriers are in **bold**. p-type barriers are doped to 1.4×10^{18} cm^{-3}.

While SIMS was used to accurately measure the doping in the contact layers in a calibration sample grown prior to the present wafer, the doping in the thin heterolayers was below the resolution of the SIMS system and prevented accurate determination of the sheet density in each period. The final capping heterolayers consisted of a 1.1 nm Si barrier, a 3.75 nm $Si_{0.5}Ge_{0.5}$ quantum well, a 0.94 nm Si barrier, a 50 nm graded $Si_{1-x}Ge_x$ collector from 0.50 to 0.534 doped at 1×10^{18} cm^{-3}, a 50 nm p-$Si_{0.66}Ge_{0.34}$ doped at 1×10^{18} cm^{-3}, and a p-Si cap also doped at 1×10^{18} cm^{-3}. This design has a miniband width of 8 meV which is nar-

rower than the radiative transition of ~12 meV to prevent reabsorption.

Samples from both grown wafers were cleaved into chips and multiple devices were processed for electroluminescence characterization. Mesas for ridge waveguide devices were etched using reactive ion etching with the Bosch process. For the first sample a 7 mm$\times$75 μm ridge waveguide demonstrated the clearest electroluminescence spectra while the low number of periods in sample 2 combined with the lower current density required five ridge interdigitated mesas to achieve the clearest electroluminescence. Ni was evaporated as a top Ohmic contact and Al as a bottom Ohmic contact. Both were annealed at 450 °C to form shallow NiSi top contacts and spiked Al bottom contacts, respectively. Transmission line measurement structures were fabricated on the same die as the electroluminescence ridges and used to obtain contact and series resistances which were subtracted from the total applied bias to allow accurate measurements of the electric fields applied across each device. The samples were back-coated with Ti/Au and indium-bonded to Ti/Au coated copper mounts to ensure good thermal contact. Fourier transform infrared spectroscopy (FTIR) was performed using a Bruker 66vs FTIR in step-scan mode with a QMC Instruments Ltd. liquid-He cooled composite Si bolometer detector. The sample was cooled using a continuous flow He cryostat with polyethylene optical windows. The voltage was applied vertically across the 100 periods on each sample with a 10 kHz square wave pulse stream at varying duty cycles, gated by a 387 Hz, 50% duty cycle square wave for lock-in purposes.[17] All parts of the system in which THz radiation propagated were either under vacuum or purged with dry N_2 to eliminate water vapor absorption. Four separate samples for each design all demonstrated nominally identical results and the measurements from a single sample of each will be presented in this paper.

Figure 4 shows the band structure for the first sample at an applied electric field of 2.5 kV/cm. The use of a higher Ge content than previous Si-based THz designs results in the LH states being pushed to much higher energy and in particular
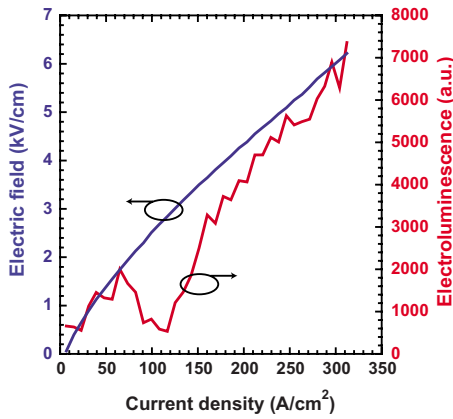
FIG. 5. (Color online) The red curve is the electroluminescence power of sample 1 and the blue curve is the electric field as a function of the current density at 4.2 K.

above the upper radiative state shown in red. Simulations of the structure demonstrate that both the hole transport and the electroluminescence from the design should be dominated by the HH states only. In addition, the narrow miniband and the high energy of the LH states produce a design in which no reabsorption of the emitted photons from the HH to HH intersubband transitions can take place. The present design as grown has the radiative subband state below the injection miniband and so the upper radiative state will be populated through incoherent transport (scattering)[33] and not through coherent resonant tunneling. This will reduce the maximum current through the device and therefore the maximum gain, although the simulations do predict a substantial current from a number of scattering mechanisms including interface roughness, ionized impurity scattering, acoustic and optical phonon scattering, and alloy scattering.[21] Figure 5 shows the luminescence-current-voltage (LIV) curve for the first sample. Below a current density of 110 A/cm^2, the electroluminescence spectra (not shown) indicate the emission is from boron impurity states.[14,34] Above 110 A/cm^2, the emitted electroluminescence power is sublinear and is predominantly related to intersubband transitions which is confirmed through the electroluminescence spectra as shown in Fig. 6.
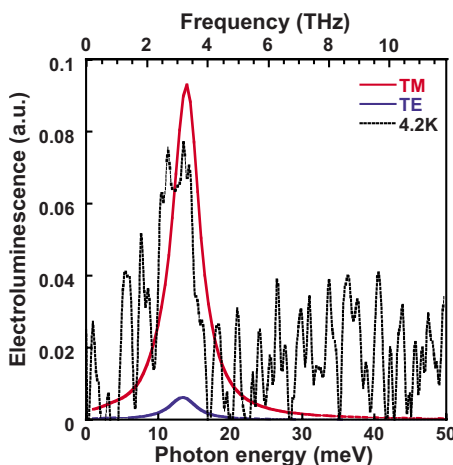

FIG. 6. (Color online) The electroluminescence spectra at 4.2 K, 3.5 kV/cm, 250 A/cm^2 for sample 1. Also plotted are the simulated spectra from 6-band **k**·**p** theory indicating the expected polarization.

The electric field versus current density (current-voltage characteristics) do not show a clear threshold voltage but rather a slow turn-on. The experimental spectra agree well with the simulated spectra calculated by 6-band **k**·**p** theory and the full-width half-maxima (FWHM) is 5 meV which is the lowest value reported for intersubband transitions in *p*-type Si/SiGe systems.[13] This agreement suggests that for this particular spectra, the emission is dominated by intersubband emission as heating would broaden the emission peak. A low FWHM is important for achieving a laser since the gain is inversely proportional to the FWHM.[13] The signal to noise ratio of the emitted power was too low to be able to accurately determine the polarization of the emitted signal.

The major problem with measuring such devices is that the high currents produce Joule heating ($=I^2R$ for current I and device resistance R) which will produce blackbody emission which may be comparable or even larger than the intersubband signal. This is particularly a problem with large FWHM emission peaks as frequently produced in the valence band through nonparabolicity but also mixing of the HH and LH states at $k_\parallel > 0$ since the FTIR interferogram then becomes narrow (the interferogram width is proportional to 1/FWHM since a Fourier transform relates the two—a delta-function emission peak has an infinite width interferogram). Once lasing has been achieved, this is not a major issue as the gain in typical QCLs results in the laser output power being around 10^6 higher than the subthreshold electroluminescence.[6] The mixing of the HH and LH states at $k_\parallel > 0$ is evident from the TE component in the theoretical spectra (see Fig. 6) which appears despite that the transition being between HH states normally only produces TM polarized emission. Intersubband spontaneous emission peaks for electrons in GaAs are typically between 0.5 and 1.5 meV[8] due to the more parabolic conduction band. Therefore it is easier to differentiate between the wide blackbody and a narrow spontaneous emission peak. For wide spontaneous emission peaks, (≥ 5 meV) the spectral width can be very similar to the blackbody emission from heating making it difficult to differentiate between the two types of emission. For the present sample, once the contact resistances have been subtracted, the active region has a resistance of between 2.5 and 3 Ω when the minibands form. In this regime, up to 1.8 A of current flows through the device producing significant amounts of Joule heating.

In Fig. 7 a comparison is made between the standard bolometer electroluminescence measurement without the spectrometer and the power extracted from spectral measurements and the blackbody spectra corresponding to the Joule heating in the system. While the vertical power scale for both are not the same, the qualitative changes as a function of voltages do match the predicted changes in the system and both have been scaled so that the total integrated power from the spectral measurements match the total bolometer reading when the spectrometer is not used for the measurement. (This can be achieved either by placing the bolometer directly in front of the cryostat with the source or running the source beam through the Michelson interferometer in the FTIR system with the two mirrors set with equal path length). At 2 V, the total integrated spectral power measure-
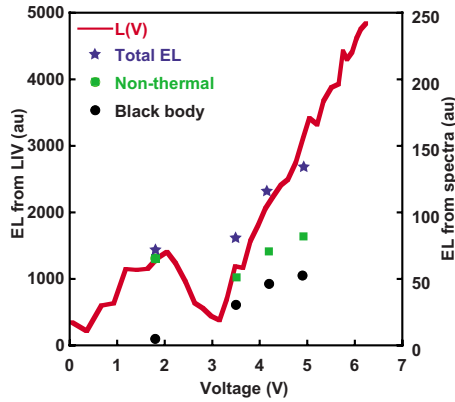
FIG. 7. (Color online) The electroluminescence power vs applied voltage at 10 K for sample 1. The solid line is the electroluminescence obtained directly from the bolometer without the spectrometer (the left-hand *y*-axis) while the dots, squares, and stars correspond to values extracted from spectral measurements (right-hand *y*-axis).

FIG. 8. (Color online) The calculated squared envelope functions for sample 2 at 7 kV/cm as calculated by 6-band **k·p** theory. The blue states are HH, the green states are LH, and the red state is one of the two upper laser level HH states. A second higher energy subband state also provides a significant contribution to the electroluminescence. The solid black line is the HH band edge and the dotted black lines is the LH band edge. The diagonal red arrow indicates the radiative transition. The germanium interdiffusion length was set to 1.0 nm for this calculation.

ment corresponds closely with the nonthermal spectra emission in the system. This emission is from impurity states which produce very narrow peaks with FWHM below 1 meV and due to the low voltage and low current there is very little heating at these biases. Therefore the spectral measurement accurately maps the total power output and the impurity electroluminescence is far stronger than any heating. Above 3 V where the impurity emission ceases, the spectra measurements indicate that a significant part of the power output as measured by the nonspectral bolometer measurements is related to Joule heating. For this particular case, the nonthermal element obtained from spectral measurements is the intersubband emission and it is greater than the blackbody emission from heating. Similar analysis for the power and spectra at 20 K (not shown) demonstrated that the impurity emission has been quenched by the higher substrate temperature and the backbody heating has become larger than the intersubband emission above 3 V. The ratio between the intersubband and the blackbody, however, will show only a small difference between the TE and TM polarized emission since the intersubband predominantly emits TM polarized light but the Joule heating will have more similar contributions from both TE and TM components. This explains the poor signal to noise resulting from the polarization measurements, as the polarizer has a significant insertion loss (Infraspecs P01 polarizer) and the large thermal emission will result in very little difference between the TE and TM modes.

The band structure for the second sample is shown in Fig. 8. Again the upper radiative states are below the ground state in the miniband which will result in incoherent transport into the bound state. For this design, the LH states are closer in energy to the upper radiative states and therefore some of the LH states may reabsorb the emitted photons. Figure 9 shows the electroluminescence power as a function of voltage for 5 different temperatures between 4 and 40 K. In the 4 K spectra, impurity state emission is also observed below about 1 V but in this sample it is weaker than in sample 1. The current-voltage curves for this sample (Fig. 10) are more linear than those in sample 1. Sample 1 has a
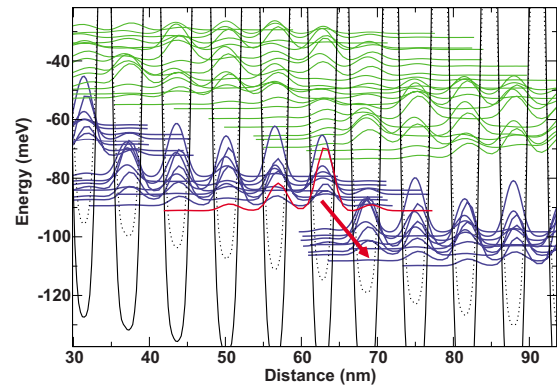
7 μm thick graded buffer which is expected to produce a lower threading dislocation density than the 3 μm graded buffer of sample 2. The near linear current-voltage for sample 2 is therefore probably related, at least in part, to the larger defect density which is qualitatively evident in optical microscope pictures of devices from the two different growth systems.

The electroluminescence spectra from sample 2 is shown in Fig. 11. Again good agreement with the theory is produced. Polarization measurements did not provide sufficient signal to noise ratio to demonstrate a dominant TM mode as predicted by theory. Theory does predict a larger TE component for sample 2 compared to sample 1 which is related to the LH states being closer to the HH states in sample 2 which creates more HH/LH mixing. The FWHM for this sample is ~5 meV which is again a low value for the *p*-type Si/SiGe system. While the spectra are very similar to sample 1, the electric field at which intersubband alignment occurs is almost twice the value for sample 2 which is related to the designs (sample 1 had wider quantum wells which results in a lower electric field for alignment).
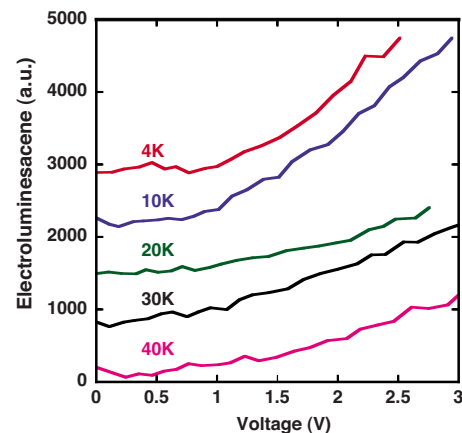

FIG. 9. (Color online) The electroluminescence vs voltage for sample 2 at temperatures between 4 and 40 K. The traces are offset vertically by 700 units for clarity.
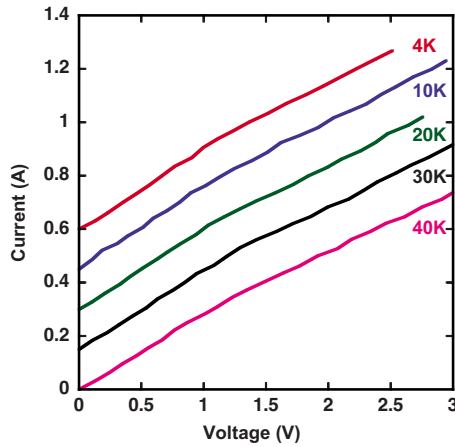
FIG. 10. (Color online) The current vs voltage characteristics for sample 2 for temperatures between 4 and 40 K. The curves are offset vertically by 0.15 A for clarity.

A Stark shifted transition energy is considered by many to be a property of intersubband quantum well lasers. The modeled electroluminescence as a function of the applied electric field for the first sample, predicts a Stark shift of 0.4 meV cm/kV. This translates to 1 meV per 1.3 V for the first sample. For the second sample the predicted shift is 0.35 meV cm/kV, which, accounting for the larger contact resistance, arrives at the same energy shift per voltage. This magnitude of shift cannot be ruled out in the devices tested in this work, although generally it is below the measurement accuracy at the current low level of output signal. It should be noted that GaAs/AlGaAs bound-to-continuum THz lasers do not always display a Stark shift during spontaneous emission[35] and so the lack of any clear and measurable Stark shift in the present samples does not preclude intersubband emission. The large devices used in this work to allow measurable intersubband signals results in our power supply being unable to deliver sufficient power to demonstrate misalignment of the minibands at sufficiently high electric fields.

The results presented above demonstrate that THz electroluminescence can be measured from *p*-type bound-to-continuum Si/SiGe quantum cascade superlattice designs
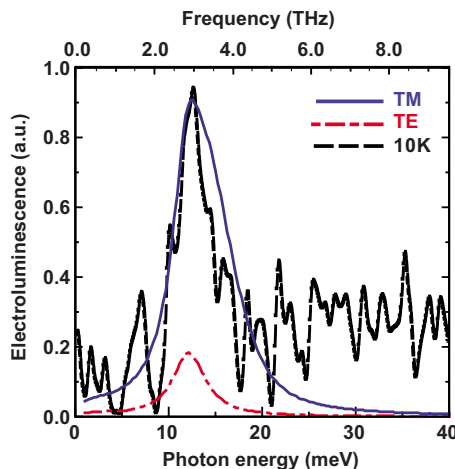

FIG. 11. (Color online) The electroluminescence spectra from the second sample at 10 K, 6 kV/cm, and 170 A/cm² compared to the TE and TM polarized spectra as calculated by 6-band **k·p** theory at 6 kV/cm.

provided that strain is used to push the LH states to energies above all the HH states used for THz emission. Theory predicts that the further away the LH states are from the HH states in energy, the less the mixing of the two and the higher the gain that can be designed into the system. Sample 1 had the LH states pushed to 25 meV (see Fig. 4) while sample 2 demonstrates that the technique is still successful at producing electroluminescence when the LH states are only ~10 meV above the HH miniband (although any gain will be smaller than sample 1). Even though the LH to HH miniband energy is comparable to the HH to HH radiative transition in the system, intersubband transitions are still observed suggesting that reabsorption between the LH states and the HH miniband is not significant. This suggests that the lack of intersubband electroluminescence in previous work which had the parasitic LH states between the HH states of the radiative transition[25] was predominantly the result of the holes being scattering (through, e.g., interface roughness, defect or Coulombic scattering) into the LH states preventing any significant electroluminescence. The second sample also had less abruption heterointerfaces than the first sample. The present results demonstrate that provided the **k·p**-modeling accounts for the nonabrupt interfaces using the correct electrostatic potential, good agreement can be achieved with the experimental intersubband emission results.

The analysis clearly demonstrates the main problems with characterization of *p*-type Si/SiGe quantum cascades which stem from the large FWHM of the spontaneous emission peak due to the nonparabolicity of the valence band which can be comparable to the blackbody thermal emission from the heating of the device. Clearly a move to electron based QCL designs which could use the more parabolic conduction bands would not only make the characterization of spontaneous emission easier but should also show significantly higher gain mainly through the lighter m^*, according to a number of proposals.[36–38] Further work has also determined that lighter m^* systems such as *n*-type Ge quantum well QCLs have more tolerance to growth fluctuations and inaccuracies[38] and a number of multiple Ge quantum well heterostructures have now been demonstrated experimentally.[39–43]

The present designs have also suffered by the upper radiative state not being inside the energy range of the miniband thereby reducing the coupling between the injector and the upper radiative state. This results in scattering being required to populate the upper radiative state thereby reducing the current through the sample and therefore the maximum gain. The optimum case is where strong coupling between the ground state of the injector and the upper radiative state exists so that the current is determined by the upper radiative state lifetime through the coherent transport in the system.[33] Such coherent tunneling designs provide a clear route to produce improvements to the present results to help improve the gain from such Si/SiGe designs.

To conclude, electroluminescence results have been presented from two different Si/SiGe superlattice designs grown by different techniques. Both samples demonstrate intersubband electroluminescence close to 3 THz. Clear electrolumi-

nescence is achieved when the minibands align at the required electric field at low enough temperatures that the electroluminescence is not swamped by thermal emission from the devices. The results demonstrate that designs which use strain to push the LH states to energies well above the radiative transition states is key to achieving THz electroluminescence in *p*-type systems. The measured FWHM of the electroluminescence peaks was 5 meV for both samples, which are the lowest reported values in the Si/SiGe system. As the experimental FWHM is comparable to the theoretical value from 6-band $\mathbf{k} \cdot \mathbf{p}$ theory, this suggests that the present width is now dominated by the nonparabolicity of the valence band. The large valence band nonparabolicity will limit further FWHM reductions and this combined with the relatively high effective mass of 0.3 m_0 may ultimately prevent sufficient gain from *p*-type Si/SiGe heterostructures to overcome the waveguide losses for a laser. We therefore believe that *n*-type germanium quantum well designs with reduced nonparabolicity and lower effective mass represent a more promising path to achieving a THz laser on a silicon substrate.

ACKNOWLEDGMENTS

[1] R. M. Woodward, B. E. Cole, V. P. Wallace, R. J. Pye, D. D. Arnone, E. H. Linfield, and M. Pepper, Phys. Med. Biol. **47**, 3853 (2002).

[2] M. C. Kemp, P. F. Taday, B. E. Cole, J. A. Cluff, A. J. Fitzgerald, and W. R. Tribe, Proc. SPIE **5070**, 44 (2003).

[3] A. J. Fitzgerald, B. E. Cole, and P. F. Taday, J. Pharm. Sci. **94**, 177 (2005).

[4] P. H. Siegel, IEEE Trans. Microwave Theory Tech. **50**, 910 (2002).

[5] M. Tonouchi, Nat. Photonics **1**, 97 (2007).

[6] R. Köhler, A. Tredicucci, F. Beltram, H. E. Beere, E. H. Linfield, A. G. Davies, D. A. Ritchie, R. C. Iotti, and F. Rossi, Nature (London) **417**, 156 (2002).

[7] B. S. Williams, Nat. Photonics **1**, 517 (2007).

[8] G. Scalari, C. Walther, M. Fischer, R. Terazzi, H. Beere, D. Ritchie, and J. Faist, Laser Photonics Rev. **3**, 45 (2009).

[9] B. S. Williams, S. Kumar, Q. Hu, and J. L. Reno, Electron. Lett. **42**, 89 (2006).

[10] M. A. Belkin, J. A. Fan, S. Hormoz, F. Capasso, S. P. Khanna, M. Lachab, A. G. Davies, and E. H. Linfield, Opt. Express **16**, 3242 (2008).

[11] S. Kumar, Q. Hu, and J. L. Reno, Appl. Phys. Lett. **94**, 131105 (2009).

[12] D. J. Paul, Semicond. Sci. Technol. **19**, R75 (2004).

[13] D. J. Paul, Laser Photonics Rev. (in press).

[14] S. A. Lynch, S. S. Dhillon, R. Bates, D. J. Paul, D. D. Arnone, D. J. Robbins, Z. Ikonic, R. W. Kelsall, P. Harrison, D. J. Norris, A. G. Cullis, C. R. Pidgeon, P. Murzyn, and A. Loudon, Mater Sci. Eng., B **89**, 10 (2002).

[15] S. A. Lynch, R. Bates, D. J. Paul, D. J. Norris, A. G. Cullis, Z. Ikonic, R. W. Kelsall, and P. Harrison, Appl. Phys. Lett. **81**, 1543 (2002).

[16] R. Bates, S. A. Lynch, D. J. Paul, Z. Ikonic, R. W. Kelsall, P. Harrison, S. L. Liew, D. J. Norris, A. G. Cullis, W. R. Tribe, and D. D.Arnone, Appl. Phys. Lett. **83**, 4092 (2003).

[17] S. A. Lynch, D. J. Paul, P. Townsend, G. Matmon, Z. Suet, R. W. Kelsall, Z. Ikonic, P. Harrison, J. Zhang, D. J. Norris, A. G. Cullis, C. R. Pidgeon, P. Murzyn, B. Murdin, M. Bain, H. S. Gamble, M. Zhao, W.-X. Ni, IEEE J. Sel. Top. Quantum Electron. **12**, 1570 (2006).

[18] P. Murzyn, C. R. Pidgeon, J.-P. R. Wells, I. V. Bradley, Z. Ikonic, R. W. Kelsall, P. Harrison, S. A. Lynch, and D. J. Paul, D. D. Arnone, D. J. Robbins, D. Norris, and A. G. Cullis, Appl. Phys. Lett. **80**, 1456 (2002).

[19] R. W. Kelsall, Z. Ikonic, P. Murzyn, C. R. Pidgeon, P. J. Phillips, D. Carder, P. Harrison, S. A. Lynch, P. Townsend, D. J. Paul, S. L. Liew, D. J. Norris, and A. G. Cullis, Phys. Rev. B **71**, 115326 (2005).

[20] C. R. Pidgeon, P. J. Phillips, D. Carder, B. N. Murdin, T. Fromherz, D. J. Paul, W.-X. Ni, and M. Zhao, Semicond. Sci. Technol. **20**, L50 (2005).

[21] M. Califano, N. Q. Vinh, P. J. Phillips, Z. Ikonic, R. W. Kelsall, P. Harrison, C. R. Pidgeon, B. N. Murdin, D. J. Paul, P. Townsend, I. M. Ross, and A. G. Cullis, Phys. Rev. B **75**, 045338 (2007).

[22] P. See, D. J. Paul, B. Hollander, S. Mantl, I. V. Zozoulenko, and K.-F. Bergren, IEEE Electron Device Lett. **22**, 182 (2001).

[23] P. See and D. J. Paul, IEEE Electron Device Lett. **22**, 582 (2001).

[24] J. Faist, M. Beck, T. Aellen, and E. Gini, Appl. Phys. Lett. **78**, 147 (2001).

[25] D. J. Paul, G. Matmon, P. Townsend, J. Zhang, M. Zhao, and W.-X. Ni, Inst. Electron. Telecommun. Eng. J. Res. **53**, 285 (2007).

[26] L. Diehl, S. Meneşe, E. Müller, D. Grützmacher, H. Sigg, U. Gensser, I. Sagnes, Y. Campidelli, O. Kermarrec, D. Bensahel, and J. Faist, Appl. Phys. Lett. **81**, 4700 (2002).

[27] Z. Ikonić, P. Harrison, and R. W. Kelsall, J. Appl. Phys. **96**, 6803 (2004).

[28] L. Lever, in *Proceedings of the Ninth International Conference on Intersubband Transitions in Quantum Wells*, edited by D. Indjin, Z. Ikonic, P. Harrison, and R. W. Kelsall (IOP, London, 2007), Vol. 9, p. 19.

[29] M. Meduna, J. Novák, G. Bauer, V. Holý, C. V. Falub, S. Tsujino, and D. Grützmacher, Semicond. Sci. Technol. **22**, 447 (2007).

[30] I. M. Ross, M. Gass, T. Walther, A. Bleloch, A. G. Cullis, L. Lever, Z. Ikonic, M. Califano, R. W. Kelsall, J. Zhang, and D. J. Paul, in *Springer Proceedings in Physics*, edited by A. G. Cullis and P. A. Midgley (Springer-Verlag, Berlin, 2008), Vol. 120, pp. 269–272.

[31] G. Isella, Solid-State Electron. **48**, 1317 (2004).

[32] Z. Suet, D. J. Paul, J. Zhang, and S. G. Turner, Appl. Phys. Lett. **90**, 203501 (2007).

[33] C. Sirtori, F. Capasso, J. Faist, A. L. Hutchinson, D. L. Sivco, and A.Y. Cho, IEEE J. Quantum Electron. **34**, 1722 (1998).

[34] S. A. Lynch, P. Townsend, G. Matmon, D. J. Paul, M. Bain, H. S. Gamble, J. Zhang, Z. Ikonic, R. W. Kelsall, and P. Harrison, Appl. Phys. Lett. **87**, 101114 (2005).

[35] C. Worral, J. Alton, M. Haughton, S. Barbieri, H. E. Beere, D. A. Ritchie, and C. Sirtori, Opt. Express **14**, 171 (2006).

[36] K. Driscoll and R. Paiella, Appl. Phys. Lett. **89**, 191110 (2006).

[37] A. Valavanis, L. Lever, C. A. Evans, Z. Ikonic, and R. W. Kelsall, Phys. Rev. B **78**, 035420 (2008).

[38] A. Valavanis, Z. Ikonić, and R. W. Kelsall, J. Opt. A, Pure Appl. Opt. **11**, 054012 (2009).

[39] M. Bonfanti, E. Grilli, M. Guzzi, M. Virgilio, G. Grosso, D. Chrastina, G. Isella, H. von Känel, and A. Neels, Phys. Rev. B **78**, 041407(R) (2008).

[40] C. Lange, N. S. Köster, S. Chatterjee, H. Sigg, D. Chrastina, G. Isella, H. von Känel, M. Schäfer, M. Kira, and S. W. Koch, Phys. Rev. B **79**, 201306(R) (2009).

[41] Y. H. Kuo, Y. K. Lee, Y. Gee, S. Ren, J. E. Roth, T. I. Kamins, D. A. B. Miller, and J. S. Harris, Nature (London) **437**, 1334 (2005).

[42] S. Tsujino, H. Sigg, G. Mussler, D. Chrastina, and H. von Känel, Appl. Phys. Lett. **89**, 262119 (2006).

[43] M. Virgilio, M. Bonfanti, D. Chrastina, A. Neels, G. Isella, E. Grilli, M. Guzzi, G. Grosso, H. Sigg, and H. von Känel, Phys. Rev. B **79**, 075323 (2009).